Characterization and distribution of mechanically competent mineralized tissue in micropores of beta-tricalcium phosphate bone substitutes

Marc Bohner, Gamal Baroud, Anke Bernstein, Nicola Doebelin, Laetitia Galea, Bernhard Hesse, Roman Heuberger, Sylvain Meille, Pascal Michel, Brigitte von Rechenberg, et al.

ELSEVIER

Characterization and distribution of mechanically competent mineralized tissue in micropores of β-tricalcium phosphate bone substitutes

Marc Bohner[1,*], Gamal Baroud[2], Anke Bernstein[3], Nicola Döbelin[1], Laetitia Galea[1], Bernhard Hesse[4], Roman Heuberger[1], Sylvain Meille[5], Pascal Michel[1], Brigitte von Rechenberg[6], Jorge Sague[1] and Howard Seeherman[7]

[1] RMS Foundation, 2544 Bettlach, Switzerland
[2] Laboratoire de Biomécanique, Faculté de Génie, Université de Sherbrooke, Sherbrooke, Québec, Canada J1K 2R1
[3] Dept of Orthopedic and Trauma Surgery, Albert-Ludwigs University Medical Center Freiburg, 79106 Freiburg, Germany
[4] European Synchrotron Radiation Facility, CS40220, Grenoble 38043 Cedex 9, France
[5] Université de Lyon, INSA-Lyon, MATEIS CNRS UMR5510, F-69621 Villeurbanne, France
[6] Musculoskeletal Research Unit (MSRU), Competence Center for Applied Biotechnology and Molecular Medicine (CABMM), Equine Hospital, University of Zurich, 8057 Zurich, Switzerland
[7] BioVentus Surgical, BU Photonics Center, Boston, MA 02215, USA

Although bone formation around and within implants has been intensively studied, the role of pores and pore geometry is still debated. Notwithstanding studies reporting the formation of bone and bone components within pores as small as a few micrometers ('micropores'), bone ingrowth is believed to only occur in pores larger than 100 μm ('macropores'). A thorough analysis of 10 different porous β-tricalcium phosphate cylinders (Ø: 8 mm; L: 13 mm) implanted for 2–24 weeks in an ovine model demonstrates ingrowth of mineralized tissue (MT) in pores as small as 1 μm. This tissue contained calcium phosphate, collagen, and interconnected cells. It formed within the first 3–4 weeks of implantation, extended over several hundred micrometers within the ceramic, and contributed to the majority of the early MT formation (including bone) in the defect. The indentation stiffness of the MT-ceramic composite was significantly higher than that of bone and MT-free ceramic. The presented results substantiate the importance of micropores for optimal bone healing, particularly at early implantation times.

Introduction

Mineralized tissues (MTs) are not only essential for such daily activities as walking, lifting, and eating, but also have an important esthetic component (teeth, face shape). Defective MTs can therefore have a dramatic impact on our functioning and well-being. The 27 EU countries spent an estimated €37 billion on treating osteoporotic fractures in 2010 [1]. Improving the management of bone healing is thus of great socioeconomic importance.

Implants have greatly advanced the treatment of musculoskeletal disorders, becoming the standard of care for diseased joints, bone fractures, and missing teeth. Bone graft substitutes are increasingly used to replace autologous bone grafts. Despite these successes, the increasing incidence of diseases impairing bone healing capacity, such as osteoporosis and metabolic diseases, requires new approaches to trigger early and intense bone formation. Current design paradigms of non-cemented implant and bone graft substitutes entail (a) a moderately rough surface (roughness Sa > 1–2 μm) [2] for the initial attachment of cells and mineralization [3], and (b) pores larger than 100 μm ('macropores') for bone ingrowth and long-term stability [4,5].

Numerous studies suggest that pores smaller than 100 μm ('micropores') might play an important role for bone ingrowth. Indeed, bone [6–8], osteoid tissue [6,7,9], mineralized collagen [9–11], collagen [11,12], and bone cells [7,12,13] have been reported in micropores. Also, increased bone formation [7,14] and accelerated bone-healing [15] have been associated with the

*Corresponding author:. Bohner, M. (marc.bohner@rms-foundation.ch)

 http://dx.doi.org/10.1016/j.mattod.2017.02.002

presence of micropores. However, there is currently no understanding of their potential mechanism of action. Lan Levengood et al. [7] suggested that 'embedded osteocytes distributed throughout microporous rods may form a mechanosensory network', but the distribution of MTs/osteocytes within the microporous space is unexplored. It is generally proposed that bone components within the micropores are the result of an 'invasion' or 'secretion' from the macropore surface rather than a cell-mediated process provoked by the presence of cells within the micropores [10,11]. In the past, we performed two ovine studies looking at the effect of macro- and microstructure on the *in vivo* behavior of β-tricalcium-phosphate (β-TCP, β-$Ca_3(PO_4)_2$) scaffolds [16,17]. Between the two studies, ten different β-TCP scaffolds were used. Tested factors included the implantation time (2–24 weeks), the macropore size (Ø 150 ± 50 μm to Ø 1020 ± 180 μm), the microporosity (11–53%), the micropore size (0.4 ± 0.1 μm to 4.2 ± 0.3 μm), and the grain size (1.2 ± 0.3 μm to 3.4 ± 0.3 μm; Fig. 1; Supplementary Data 1), whereas the macroporosity was kept in a narrow range of 75 to 84%. These two *in vivo* studies provide an excellent basis to investigate the effect of micropore size and microporosity on the bone healing process, and in particular to determine the amount and location of MTs found within the micropores. For that purpose, histological sections/blocks of the two studies were analyzed by light microscopy, white light interferometry, scanning electron microscopy (SEM), energy-dispersive X-ray spectroscopy (EDX), Fourier-transform infrared spectroscopy (FTIR), instrumented indentation, and nano-computed tomography (nCT). Histomorphometrical results were assessed using an 'effective implantation time' (EIT), which allowed combining the results of the two studies.

Methods

Two large ovine studies evaluating CaP implants with varying macro and microporosity and varying composition were revisited with the specific aim to detect and characterize the MTs found in the ceramic micropores. Four β-TCP scaffolds varying in macropore size were tested in the first study [17]. The second study evaluated one monetite scaffold, one β-TCP granule, and 6 β-TCP scaffolds varying in micropore/grain size and microporosity [16]. Both studies involved the use of 8 mm × 13 mm CaP cylinders. In the first study, the CaP cylinders were implanted in bilateral core defects placed in the proximal humerus, proximal tibia, proximal and distal femur. In the second study, bilateral distal humerus defects were substituted for the proximal tibia defects [18]. Importantly, empty defects remain practically empty after 8 weeks of implantation [19]. In order to evaluate each specific CaP configuration 6 times at 3 different implantation times, 9 and 18 sheep were required for the first and second studies, respectively. Animals were euthanized at 6, 12, and 24 weeks following implantation in the first study [17]. Animals were euthanized at 2, 4, and 8 weeks following implantation in the second study [16]. Details of the implantation and explanation procedures can be found elsewhere [16,17]. An overview of the materials can be seen in Fig. 1 and Supplementary Data 1.

The β-TCP samples A to D were produced using CaP emulsions [20], resulting in fully-interconnected micropores, and partly interconnected macropores. The DCP samples were synthesized by the reaction of α-TCP macroporous block produced using CaP emulsions and phosphoric acid [21]. Macropore interconnections created during α-TCP synthesis were partially closed during the conversion reaction. Samples mg, Mg, mG, MG, Y and T were obtained by pressing a mixture of polyethylene glycol beads and tricalcium phosphate powder, and subsequent sintering. Macropores were barely interconnected (Fig. 1: Supplementary Data 1).

Thick (30–40 μm) plastic histological sections (resin: LeicaTM HistoDur, Leica Instruments GmbH, Germany) from the previous two studies surface stained with toluidine blue (TB; pre-etching with acetic acid) were newly imaged at 50× enlargement under light microscopy (Leica DMI5000 M, Leica Instruments GmbH, Germany). The resulting images were stitched together to obtain high resolution images of the entire specimen, thus allowing a more accurate spatial distinction of the various phases present within the samples (bone, ceramic, soft tissue). The same procedure was adopted with scanning electron microscopy (SE and BSE mode; EVO MA 25, Carl-Zeiss SMT AG, Oberkochen, Germany) after coating the histological sections with a carbon layer (SCD 050, BAL-TEC, Balzers, FL). Selected sections were polished with a 0.5 μm diamond paste to remove the carbon coating and the TB stain. These sections were then imaged by differential interference contrast light microscopy (Leica DMI5000 M, Leica Instruments GmbH, Germany). Some sections were analyzed by FTIR in ATR mode (LUMOS FTIR, Bruker Optics Inc., Ettlingen, Germany; Supplementary Data 2), stained with methylene blue/basic fuchsin instead of TB to better visualize cells in the MT, and/or coated with carbon to take new SEM images. Ca, P, and C elemental maps were collected with EDX (Oxford EDX X-Max, Oxford, UK).

Selected histological blocks were polished with a 0.5 μm diamond paste, coated with a thin carbon layer, and observed by SEM-SE and SEM-BSE. The topography of two selected samples was investigated using white light interferometry (S neox from Sensofar, Spain, SensoSCAN software, Version 6.1.3, Sensofar, Spain) using the 20× and 50× objectives. Stitching was performed to enlarge the field of view. Data processing was performed with the software SensoMAP Premium (Version 7.3.7690, Digital Surf, France). A MT-rich Ø 0.5 mm × L 2 mm cylinder was milled from size D block (6 weeks implantation) and evaluated with phase-contrast nano computed tomography (nanoCT) on beamline ID16B (ESRF, Grenoble, France) [22] following the protocol described elsewhere (Supplementary Data 3) [23]. The energy of the beam was set to 29.6 keV to allow for both sufficient transmission and good contrast. A LSO:Tb 17 μm thick scintillator was used to convert the X-rays into visible light which was then recorded using a PCO camera (PCO.edge 5.5, Kelheim, Germany). The sample was first scanned at a voxel size of 240 nm to obtain an overview image of the sample, using only 1251 projections of 0.25 s each to keep the imaging dose low [24]. This image was used to select a region of interest in the sample, which was then scanned with a higher resolution. The field of view corresponding to the chosen settings was approximately 100 μm in diameter and height. The histological block used for the nanoCT measurement was mechanically tested by instrumented indentation in ambient temperature using a G200 apparatus (Agilent, USA; Supplementary Data 4) to determine Young's modulus and hardness. Strain controlled ($0.05\ s^{-1}$) tests were conducted with a spherical diamond tip (nominal radius 50 μm). A CSM (continuous stiffness measurement) module was used to calculate the evolution of properties with penetration depth. Thermal drift was measured after each test and correction

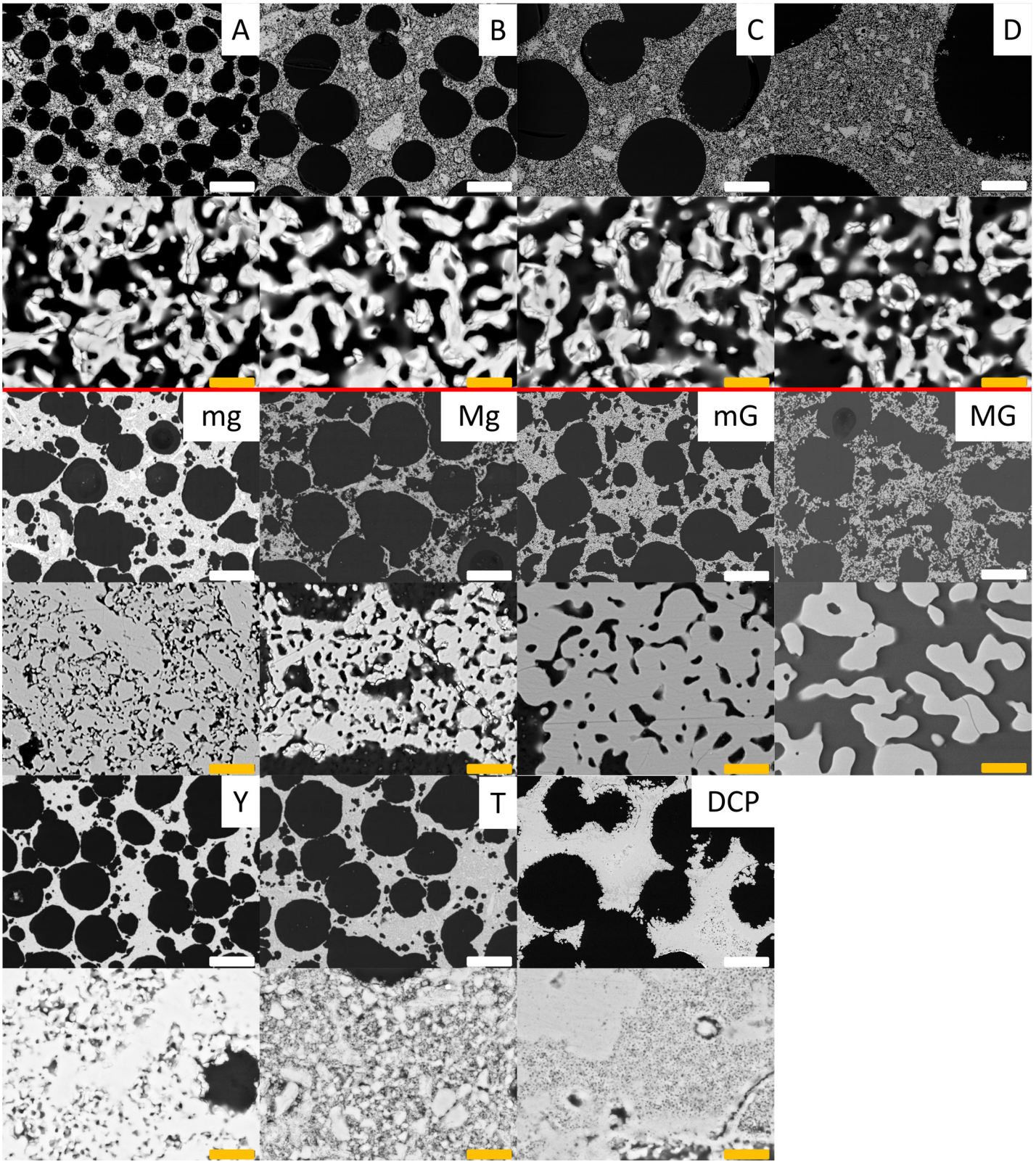

FIGURE 1

Macro and microstructure of resin-embedded and polished β-TCP ('A' to 'T') and DCP scaffolds as seen under SEM-BSE. Two images are provided per sample. The upper image (scale bar: 200 μm) contains the sample denomination and shows the macrostructure; the lower image (scale bar: 10 μm) gives details about the microstructure. The ceramic is white, and the porosity is black. The red line delimitates samples used in the two animal studies. In the first animal study, samples A to D were implanted for 6, 12, and 24 weeks [17]. In the second animal study, samples 'mg' to 'DCP' were implanted for 2, 4, and 8 weeks [16]. The sample called 'DCP' consists of monetite or anhydrous dicalcium phosphate ($CaHPO_4$).

applied. Tests were located on target zones determined from the BSE image obtained at SEM. An optical microscope and SEM were used to observe the different indents in order to verify the location of the indent (and the corresponding zone of the sample). Maximum penetration depth was 2.2 μm to have an average characterization of the tested zone (circular contact radius of approx. 14 μm). The tip area function $A(h_c)$ (projected area of the indenter as a function of the contact depth h_c) was measured by AFM. The frame compliance was calibrated before each set of experiment using a reference fused silica sample.

More details of the experimental procedures can be found in the Supplementary Data.

Results and discussion

The evaluation of TB stained histological sections of the core defects from both studies demonstrated a progressive increase of the fraction of dark blue stained (TB+) tissues from the periphery of the defect to the central region (Fig. 2). In samples mg, Y and T, TB+ tissues were only found on the ceramic macropores walls ('contact osteogenesis'). In samples A, B, C, D, and MG, the TB+ tissues were also detected in the ceramic micropores. These tissues formed with the TB+ tissues present within the macropores a trabecular structure (Fig. 2). The 2D trabecular thickness and distance between trabeculae increased with from ≈50 to 100 μm after 2 weeks of implantation to ≈500 μm after 12 weeks of implantation. Comparative staining experiments revealed that TB+ tissues were fuchsia using methylene blue-basic fuchsin stain (BF; BF positive stain [BF+], Fig. 3e; Supplementary Data 5) and green using Goldner Trichrome stain (GT; GT positive stain [GT+], Fig. 4b–e; Supplementary Data 6), the colors expected for bone with these stains. TB+ tissues within macropores had the appearance of bone, with the presence of cells within the bone and lining newly-formed bone (Supplementary Data 7).

Characterization of TB+ tissues in the ceramic micropores

The TB+ tissues found in Ø 2.6–2.9 μm micropores of scaffolds A–D (Fig. 1; Supplementary Data 1) were characterized by various means with the general aim to detect the main components of bone including calcium-phosphate (CaP) minerals, collagen, and interconnected cells.

CaP minerals were identified by a combination of SEM-BSE images and EDX measurements. SEM-BSE images of the histological sections revealed that the radio-density of the TB+ stained trabecula-like structures within the ceramic micropores was higher than that of adjacent unstained ceramic micropore regions (Fig. 3b), due to the presence of a radiodense tissue formed within the ceramic micropores (Fig. 3g). The EDX analysis demonstrated that this radiodense tissue consisted of phosphorus (P, Fig. 3j) and calcium (Ca, Fig. 3k), with minimal amounts of carbon (C, Fig. 3h). The Ca/P molar ratio of the radiodense material within the micropores was 1.83 ± 0.02, a typical value for bone mineral [25]. The Ca/P molar ratio of the unresorbed β-TCP ceramic was significantly lower (1.62 ± 0.02, $p < 0.001$; Supplementary Data 7), but still higher than the theoretical ratio of 1.50. This difference is reasonable given the limited accuracy of EDX.

Collagen was detected within TB+ tissues found in the micropores of scaffold D using the following analyses: FTIR of a polished stain-free histological section revealed amide (C=O and N–H bond) signals (Fig. 3c); all characteristic peaks of collagen were identified (Supplementary Data 2); positive staining with TB, GT and BF confirmed the presence of polyanionic molecules such as collagen; and SEM-BSE images of the interface between mineralized and non-mineralized microporous ceramic zones showed that TB+ tissues were made of mineralized fibers (Fig. 3i). The presence of collagen within ceramic micropores has also been previously reported in the literature [11,12].

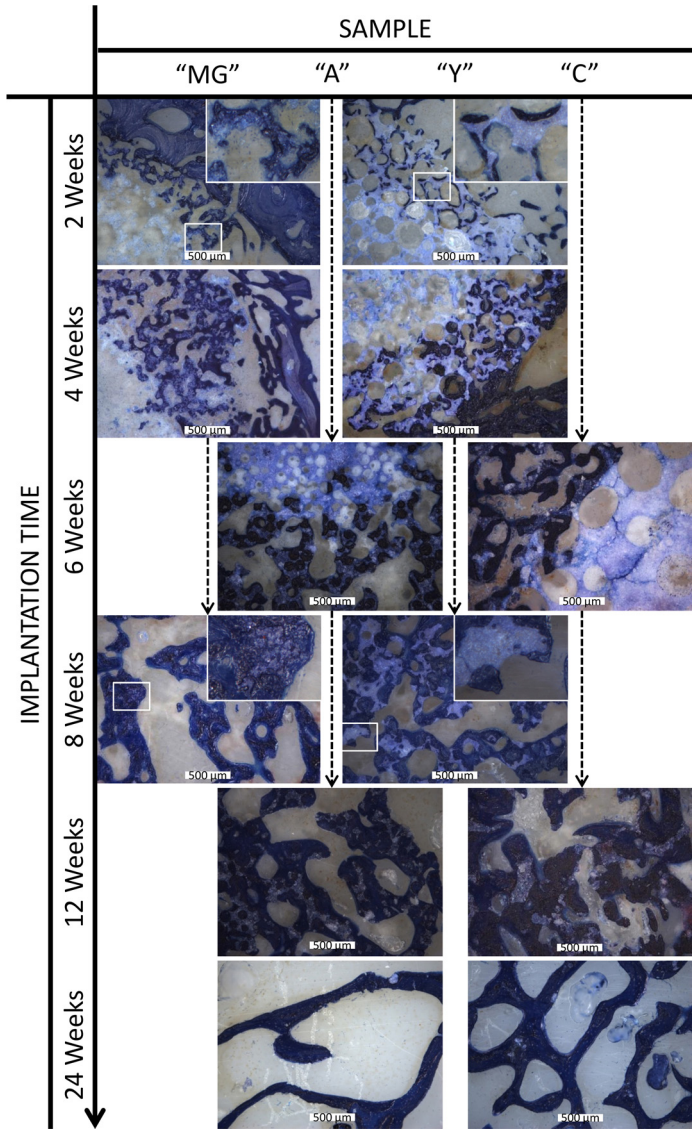

FIGURE 2

Representative images of histological sections stained with toluidine blue. Images of β-TCP samples 'MG', 'A', 'Y' and 'C' are shown after different implantation times (2–24 weeks). Dark blue: bone or mineralized tissue (MT); light blue: ceramic; yellowish gray: soft tissue. Scale bar: 500 μm. The inserts in the images at 2 and 8 weeks show details of the histological sections. In 'MG', MT (TB+ tissue) was found within the micropores; in sample 'Y', TB+ tissues were only found in the macropores, the ceramic acting as surface template.

Cells were found throughout the ceramic micropores, either in or outside TB+ areas (Fig. 4). The cells within TB+ areas appeared to be mononucleated, and had a star-like appearance with numerous processes extending between ceramic and TB+ areas (Fig. 4h; Supplementary Data 5). In TB− areas, mononucleated and multinucleated giant cells (MNGC) were observed. The MNGC were

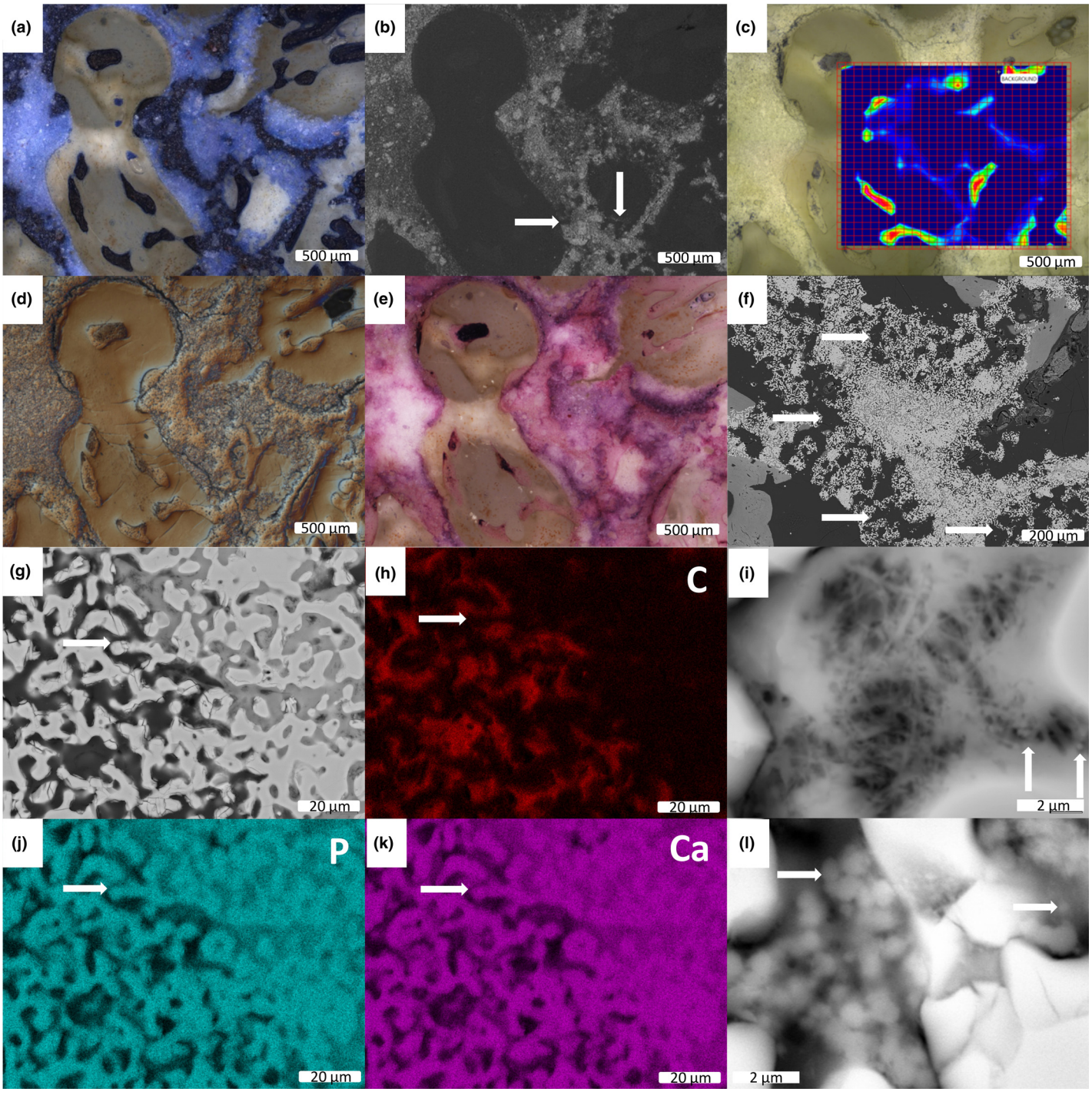

FIGURE 3

Various images of sample 'D' after 6 weeks of implantation. (a) Toluidine blue staining. Dark blue: bone and mineralized tissue (MT); light blue: ceramic free of MT; yellowish gray: soft tissue; (b) same as (a) under SEM-BSE; white: radiopaque material; Arrows: resorption pits; (c) FTIR map of sample (d) showing the protein content (blue = low content; white = high content); (d) differential interference contrast light microscopy image of sample shown in (a) after polishing; the color is a function of the sample height; (e) sample shown in (d) stained with basic fuchsin; bone and MT are colored in fuchsia; (f) SEM-BSE image of a zone containing lots of resorption pits and tunnels (arrows); (g) SEM-BSE image at the interface between MT-free and MT-filled ceramic; the arrow indicates the location of a ceramic grain; (h) carbon map of the image shown in (g); red = high content; (i) fibrous mineralized zone at the interface between MT-free and MT-filled ceramic micropores; the arrows show spherical radiopaque particles; (j) phosphor map of the image shown in (g); green = high content; (k): calcium map of the image shown in (g); violet = high content; (l) spherical radiopaque particles at the mineralizing front. The scale bars have a length of (a–e) 500 µm, (f) 200 µm; (g,h,j,k) 20 µm, and (i,l) 2 µm.

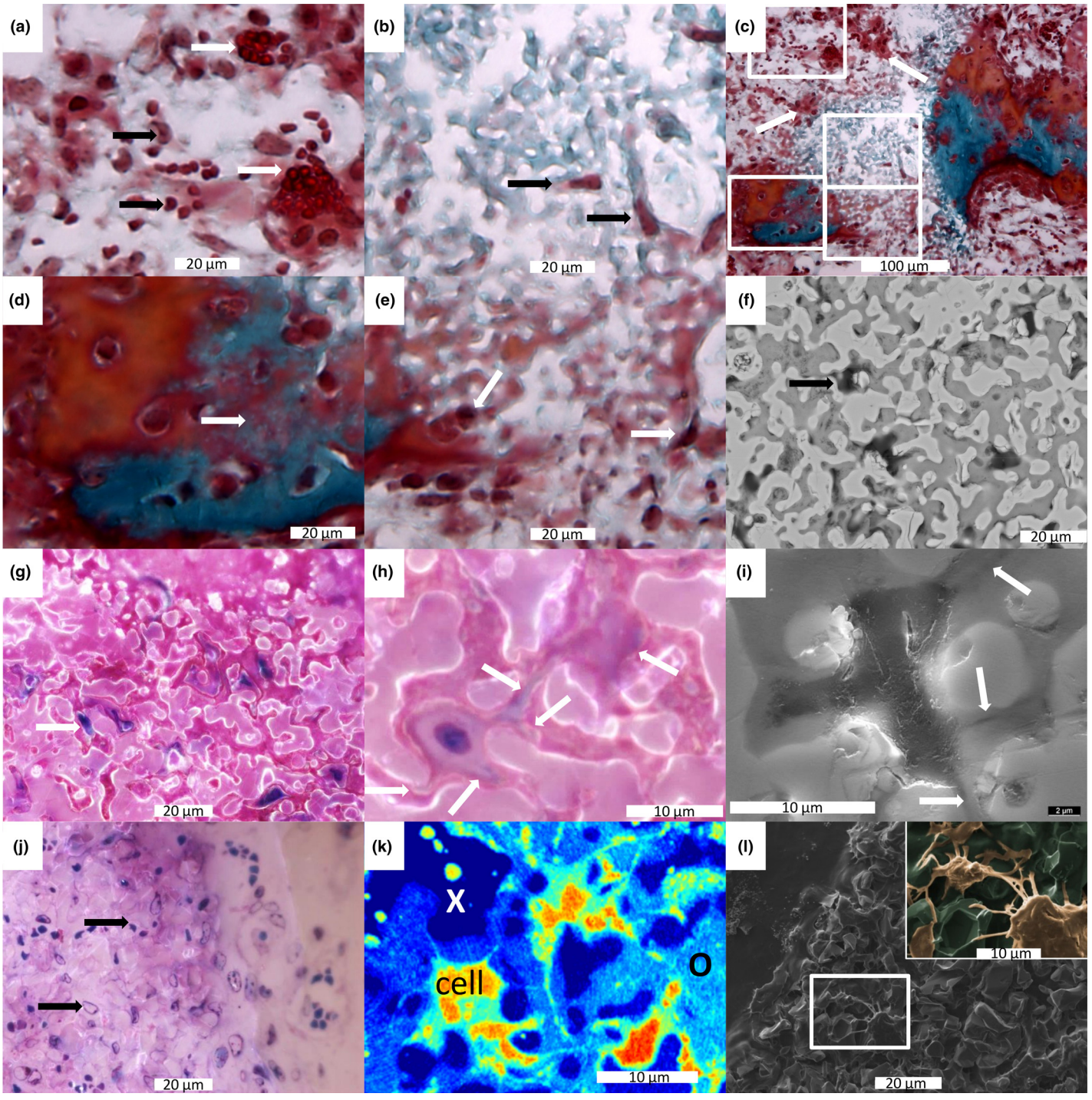

FIGURE 4

Cells present within the micropores of sample D. (a–e) Goldner trichrome (GT) stains bone in green, osteoid tissue and cell cytoplasms in red; the ceramic remains white. (a) Black arrows: two mononucleated cell morphologies seen in GT-microporous ceramic; white arrows: blood capillaries. (b) Arrows: cells present within the micropores filled with mineralized tissue (MT). (c) Arrows: multinucleated giant cells; the frames show the position of the enlargements shown in (a), (b), (d) and (e); (d) dotted green pattern typically seen during woven bone mineralization; (e) osteoid within the micropores; the arrows point toward two cells; (f) SEM-BSE image of MT-filled micropores, with some pores allocated to the presence of cells embedded in MT; (g,h) basic fuchsin staining of MT-filled ceramic micropores; (h) detail showing a cell embedded between ceramic and MT; cell processes are indicated with arrows; (i) SEM-SE image of such a cell; the arrows show cell processes; (j) basic fuchsin staining of MT-free ceramic micropores; (k) nanoCT image of cells within MT ('O') and ceramic ('X'); cells have generally two different radiopacities leading to two different colors: orange-red in the center and green on the outside: (l) cell interconnections in MT after acid etching; ceramic remnants are less dissolved than bone and MT; colors in the insert are added to ease the visualization of the interconnections. The scale bars have a length of (c) 100 µm, (a,b,d,e,f,g,j) 20 µm, and (h,i,k,l) 10 µm.

generally close to the TB+/BF+/GT+ microporous regions, in pores not present before implantation (Fig. 4c; Supplementary Data 6). These results suggest that the pores were created by the action of these MNGC. The 2D width of the cavities and tunnels created in these regions was typically close to 20–50 μm (Supplementary Data 8). Small blood capillaries could also be found (Fig. 4a). Different mononucleated cell morphologies were observed in non-mineralized micropores (Fig. 4a,j). Subsequent imaging of adjacent histological sections demonstrated that cells were present deep in the ceramic (Supplementary Data 6). The latter result was independent of the liquid used for impregnating the sample prior to implantation (blood in the first ovine study [17], 0.9% saline solution in the second study [16]), suggesting that cell migration into the micropores occurred post-implantation.

To summarize, TB+ tissues present within ceramic micropores contained the three components of bone, namely calcium phosphates, cells, and collagen. Further in the text, 'MT' is used to describe the MT present within the ceramic micropores, and 'bone' to describe the bone formed within the macropores.

Cells within the micropores

Cells within the ceramic micropores of sizes A to D were generally bigger than the micropore interconnections. However, their ability to deform [26] and the presence of numerous 10 μm large micropores within the ceramic may explain their presence in the microporous space [13]. Finding cells within the micropores raises the question of the minimum pore size allowing cell invasion and subsequent MT formation. Based on our data, the threshold size is between the micropore sizes of samples 'mg' (0.44 ± 0.02 μm), 'Y' (0.58 ± 0.03 μm), 'T' (0.41 ± 0.07 μm), and those of samples 'A' to 'D' (2.62 ± 0.44 to 2.86 ± 0.13 μm; Figs 1 and 2; Supplementary Data 9). Therefore, it seems reasonable to conclude that cell invasion and MT formation require interconnected micropores with a mean size larger than ≈1 μm. Additionally, some pores should be able to accommodate mononuclear cells which have according to our histological sections a diameter of 2–10 μm before MT formation, and almost 10 μm after MT formation (Fig. 4).

Cells within the micropores must rely on O_2, nutrient and waste diffusion to survive. Since blood capillaries (Ø 25–34 μm; [27]) are too large to penetrate the microporous space, a passive diffusion-controlled mechanism must account for this transport. A critical distance is 100–150 μm. Indeed, cell hypoxia occurs 100 μm or more from blood capillaries [28]. In cortical bone, lacuna-canalicular network osteocytes are found 150 μm away from a blood vessel [29]. In cancellous bone, no blood vessels are present within the 190 ± 50 μm thick trabeculae [30]. In the current study, the mean intercept length in the trabeculae-like structure within the microporous space was not greater than 100–120 μm (Fig. 5e), suggesting that requirements for O_2, nutrient and waste diffusion were fulfilled.

Osteoid seams found in macropores were sometimes seen to penetrate into or even cross microporous ceramic domains (Fig. 4c,e), although the seams appeared broader and the cells were less aligned in the ceramic than in the macropores (Fig. 4e, Supplementary Data 6). Tissue mineralization seemed to proceed via the nucleation and growth of spherical mineralized particles, as described by Bosshardt and Schenk for woven bone formation [31]. Indeed, mineralized spheres with a size anywhere between 50 nm and 1–2 μm were found within the micropores (Fig. 4i,l; Supplementary data 9). The cells found within the mineralized regions had a different morphology (Fig. 4g,j; Supplementary Data 5), which may suggest a phenotype change during mineralization. The size of the MT-embedded cells was estimated from the size of the pores present in the ceramic-MT composite as seen by SEM-BSE (Fig. 4f,i); it was not statistically different from that of cells typically embedded in bone (osteocytes: $p = 0.22$, Supplementary Data 10). However, the cells' shape differed slightly. In our two studies, cells were more elongated and concave, due probably to the geometrical constraints of the ceramic micropores. Canaliculi were difficult to detect with conventional histological staining, but cell processes were present (Supplementary Data 5, 10). The osteocyte nature of MT-embedded cells is best confirmed using a sclerostin marker. Unfortunately, all bone samples were already impregnated in a resin inadequate for immuno-histochemical investigations. Instead, an attempt was made to demonstrate that these cells were connected. Specifically, a cylinder (Ø 0.5 mm × 2 mm) of MT-ceramic composite was excised from a histological block and scanned by nCT at 50-nm resolution. Submicrometer-sized elongated channels were observed protruding from the larger cell-filled cavities (Fig. 4k, Supplementary Data 3, Supplementary Video 1), but these channels often stopped between two cells. However, interconnections between cells were seen by SEM after etching a histological block [32] (Fig. 4l; Supplementary Data 11). The cell interconnections had a diameter of 360 ± 140 nm, which is close to the reported value for canaliculi (290–440 nm [33]).

MT role in the bone healing process

A crucial question, for practical purposes, is the MT role of in the bone healing process. To address it, all histological sections stained with TB were analyzed for the thickness and volume fraction of bone, MT, and ceramic on concentric circles of 1–7 mm in diameter. No significant difference in bone and ceramic content was measured between groups A to D at 6 and 12 weeks of implantation (Supplementary Data 12), which agrees with past analysis [17]. Interestingly, after pooling the results of groups A to D at 6-week implantation, the TB+ volume fraction was found to decrease linearly ($r^2 = 0.99$, Supplementary Data 12) while moving into the scaffold, with the intercept with the diameter axis at 0.56 mm. In fact, the healing process appeared to be summarized chronologically when moving from the inner part of the defect outwards: more intact ceramic, thinner trabeculae, and more woven bone in the inner parts; more ceramic resorption, thicker trabeculae, and more lamellar bone in the outer parts of the defect. Assuming that the healing response is delayed by the distance from the implant surface, likely because of the time it takes for cells to invade the implant, each location in the scaffold could be related to an EIT. Accordingly, all results obtained at 6, 12, and 24 weeks were displayed in one figure (Fig. 5a–c). The continuity of the experimental points for the bone fraction (Fig. 5a), ceramic fraction (Fig. 5b), and mean bone intercept (Fig. 5c) validates our new pooling approach. The centripetal rate of bone formation was ≈89 μm/day, which is close to progression rate of bony spicules of 73 μm/day reported by Winet et al. [34].

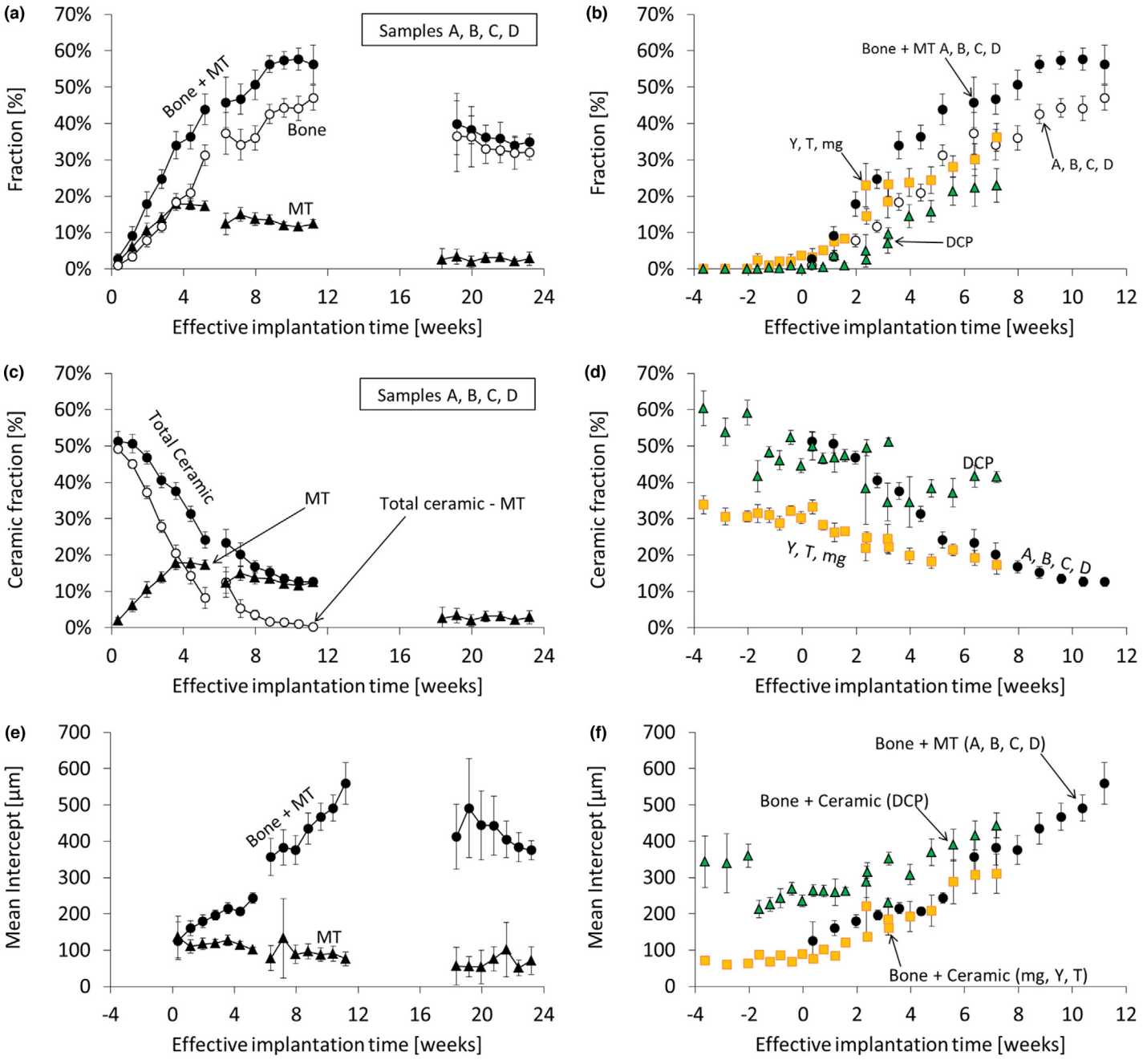

FIGURE 5

Histomorphometry results; showing (a,b) the bone and mineralized tissue (MT) fraction, (c,d) the ceramic fraction, and (e,f) the mean intercept as a function of the 'effective implantation time' (EIT) which is calculated from the implantation time and the centripetal bone ingrowth rate. In (a): (▲) MT, (○) bone, and (●) MT + bone content of samples A to D. In (b): (○) bone and (●) MT + bone content of samples A to D; bone content of (■) samples mg, Y, and T, and (▲) DCP. In (c): (▲) MT, (○) MT-free ceramic (=total ceramic content − MT), and (●) total ceramic content of samples A to D. In (d): total ceramic content of samples (●) A to D, (■) mg, Y, and T, and (▲) DCP. In (e): mean intercept of (▲) MT and (●) MT + bone. In (f): mean intercept of (●) MT + bone for sizes A to D; (■) ceramic + bone for samples mg, Y, and T, and (▲) ceramic + bone for sample DCP. The error bars correspond to ±1 standard error.

Interestingly, three domains are distinguishable in the graph relating bone/ceramic fraction and EIT for sizes A to D (Fig. 5a,b). During the first 4 weeks the MT and bone fractions increased proportionally, but slightly more MT was formed than bone. There was also a corresponding rapid reduction in the total ceramic fraction % during this time period (Fig. 5c,d). From 4 to 10 weeks the increase in TB+ fraction (=MT + bone) was primarily due to the increase in bone. The majority of the MT-free ceramic ('Total ceramic – MT' in Fig. 5c) was resorbed at the end of this period. From 10 to 24 weeks the total bone fraction decreased to the baseline value reported for this ovine model (30–35%). The MT fraction was only 2–3%. These results were verified by inspecting the histological sections' images (Fig. 2).

Samples of the second ovine study ('mg' to 'DCP'; Fig. 1) were then subjected to the same morphological analysis. No significant difference in bone fraction, ceramic fraction, and intercept was measured among the three scaffold groups of the second study which did not contain any MT (samples 'mg', 'Y', 'T'; mean

micropore size 0.41–0.58 μm; Supplementary Data 12) [16]. After pooling the results of these three groups, the TB+ fraction of samples mg, Y, and T was significantly smaller ($p = 0.0008$; Supplementary Data 13) than that of the scaffold groups A to D with Ø 2.6–2.9 μm micropores but varying macropore size (Ø 150–1020 μm) (Fig. 5b). However, the bone content was identical (Fig. 5d,f). Also, and remarkably, the trabecular network formed by the bone and the ceramic had the same dimensions as the TB+ network found in samples A to D (Fig. 5f), suggesting that the contact osteogenesis seen in samples mg, Y, and T was not a random process. The group MG (micropore size 4.15 ± 0.32 μm) had similar bone content as samples A to D, whereas groups mG and Mg presented values closer to the means of the groups mg, Y, and T (Supplementary Data 12). However, the standard deviations were too large to draw statistically significant conclusions. The finding that ceramic was removed and replaced by bone in a similar manner across the groups was surprising considering the large variations of the micro- and macrostructures of the different groups studied, including the macropore size (groups A to D), macropore interconnectivity (lower for mg, Mg, mG, MG, Y, and T than for A, B, C, and D) and macropore interconnection size ($A < B < C < D$) [16,17,20,35]. This is also surprising considering that sub-micrometric features of β-TCP scaffolds are sometimes associated with an osteoinductive response [36]. Nevertheless, significantly lower bone formation with DCP samples (Fig. 5; Supplementary Data 13) and apatitic CaP cements (Supplementary Data 14) [37] indicates that the model is sensitive enough to detect differences between scaffolds.

Postulating that MT presence should have important temporal biomechanical effects, instrumented indentation tests were performed on a histological section (size D, 6 weeks of implantation). The results showed that MT zones (Young's modulus $E = 31 \pm 9$ GPa) were much stiffer than MT-free PMMA-filled ceramic zones ($E = 16 \pm 5$ GPa; $p < 0.001$; Supplementary Data 4, 5). In comparison, the Young's moduli for both old bone and new bone were measured to be $E = 11 \pm 1$ and $E = 6 \pm 2$ GPa, respectively. Evaluation of surface irregularities using differential interference contrast light microscopy (Fig. 3d) suggested that MT zones were more abrasion-resistant than ceramic or PMMA. This result was indeed confirmed by white light interferometry (Supplementary Data 11).

In the current study, β-TCP cell-mediated resorption (Supplementary Data 8) occurred faster than that of DCP. This is a surprising finding because β-TCP is less soluble than DCP in physiological conditions (serum pH 7.4) [38,39]. XRD and EDX measurements made on histological sections showed that DCP, which appears to be also resorbed by cells (Supplementary Data 8), did not convert into more stable apatite *in vivo*. Therefore, the faster resorption rate of β-TCP compared to DCP is attributed to its higher solubility at the local pH environment created during osteoclast-mediated resorption (~4.5) [40].

To summarize, the main observations made in this study were:

- A cell-rich collagen-rich MT was found in the interconnected micropores of the β-TCP scaffolds provided the micropores were larger than a threshold value in the range of 1–10 μm.
- The ceramic in MT zones had the same micropore size and morphology as that prior to implantation (Figs 1 and 4). So, MT formation occurred without concomitant ceramic resorption.
- TB+ zones (bone + MT) formed a trabecular network which size and surface area was not affected by the macropore size of the β-TCP scaffolds (Fig. 5; Supplementary Data 12).
- MT adopted the same color as bone with three different bone stains, namely TB, methylene blue and basic fuchsin, and Goldner trichrome (Figs 3 and 4).
- The cells present in the MT were connected by thin processes having a diameter of 360 ± 140 nm, which is in the range of canaliculi diameters [33].
- MT mineralization occurred via the nucleation and growth of spherical mineralized particles, which is typically observed during woven bone formation [31].
- Three domains were observed during the healing process of bone defects filled with microporous β-TCP scaffolds: a rapid increase in MT and bone in the first 4 weeks, a slow decrease of MT and fast increase of bone fraction from 4 to 10 weeks, and a decrease of MT and bone from 10 to 24 weeks.
- MT areas were more mechanically competent than bone or ceramic areas.

Based on the observations made in this study, a number of very important questions can be answered:

1. Is MT formation chemically-driven?
2. Is MT formation controlled by processes occurring within macropores?
3. Is MT formation the result of a coordinated action of cells?
4. Is MT bone?

If MT formation was chemically-driven, one would not expect to see differences between small or large micropores. Here, no MT was observed in samples mg, Y, and T, contrary to samples with larger micropres, like A, D, or MG. Also, elongated patterns crossing microporous regions would not be expected, contrary to what was observed in e.g. sample D (Figs 2 and 3a). We would rather expect mineralization along the edges of the macropores. Furthermore, apatite does not spontaneously precipitate (not 'bioactive') onto the β-TCP ceramics *in vivo* [41,42]. So, MT formation must be biologically/cell driven.

If MT formation was controlled by processes occurring within macropores, as suggested by several authors [10,11], more MT should be found in sample A than sample D because the macropore surface area of sample A is roughly one order of magnitude larger than that of sample D. Experimentally, no statistical difference was observed between samples A, B, C and D. So, MT formation cannot be associated with 'osteoconduction' or 'contact osteogenesis' at the macropore surface. It appears therefore that MT formation is driven by the presence of cells within the micropores.

If MT formation was the result of the individual action of single cells, MT should have a dotted pattern (1 cell, one dot) and should be distributed throughout the microporous ceramic. The elongated trabecular-like patterns extending over hundreds of micrometers (Fig. 3a) and the presence of cell interconnections (Fig. 4l) suggests that MT is not produced by the individual action of single cells, but by a coordinated action of cells.

The last and most important question addressed here is: is MT bone? As bone, MT is produced by the coordinated action of cells. As bone, it contains hydroxyapatite, collagen, and interconnected cells. However, since all bone samples are embedded in plastic, it is not possible to determine the nature of the cells present within the micropores. As such, the question cannot be univocally answered.

Bosshardt and Schenk [31] described two healing phases in bone defects: (i) woven bone formation with subsequent reinforcement 'by concentric filling of the spongework lattice with primary parallel-fibered bone', and (ii) remodeling. Importantly, woven bone formation starts within a couple of days, is initiated by matrix vesicles, is completed within 4 weeks, and is not preceded by osteoclastic resorption [31]. Experimentally, MT formation started within a few days, its mineralization occurred by the nucleation and growth of spherical mineralized particles, was only produced within the first 4 weeks of implantation (Fig. 5a), and occurred without β-TCP resorption. Therefore, it is proposed that MT presence in the ceramic micropores is due to woven bone ingrowth.

Mayr et al. [43] implanted microporous β-TCP scaffolds similar to samples A to D but without macropores in a sheep femoral condyle. They observed a much slower resorption and bone ingrowth than in the present study. After 52 weeks, only 81% of the ceramic was resorbed. For comparison, only a few percent of samples A to D were left after 24 weeks implantation (Fig. 5c). This difference is attributed to the macroporosity which allowed blood vessel ingrowth required for lamellar bone formation.

Conclusion

MTs consisting of calcium phosphate, collagen, and interconnected cells were found to form in a trabecular-like pattern over hundreds of micrometers in the microporous walls of macroporous β-TCP ceramics. MT formation was driven by the coordinated action of cells within the micropores. Accordingly, MT was only found when the micropore interconnections and sizes were larger than about 1–10 μm. MT formation presented analogies to woven bone formation: it started within a few days, its mineralization occurred by the nucleation and growth of spherical mineralized particles, it was only produced within the first 4 weeks of implantation, and occurred without β-TCP resorption. Therefore, it is proposed that MT presence in the ceramic micropores is due to woven bone ingrowth.

Author contributions

MB: study design, image and data analysis, light microscopy images, data interpretation, article draft. GB: study design, data interpretation, article draft. AB: study design, data interpretation. ND: image and data analysis, data interpretation. LG: study design, electron microscopy images, data interpretation. BH: nanoCT analysis. RH: white light interferometry measurements. SM: indentation tests. PM: sample preparation, image and data analysis, light microscopy images; BR: animal studies. JS: FTIR analysis. HS: study design, data interpretation, article draft.

Acknowledgements

The authors would like to thank the following: N. Biedert and C. Delfini for light microscopy images; C. May for statistics; S. Tadier for SEM images; A. Lau, O. Loeffel, and F. Bigolin for their technical support for light microscopy, electron microscopy, polishing, and EDX measurements; J. Villanova and J.-P. Suuronen for their support during acquisition of the nanoCT data; O. Guiraud for 3D visualization; D. Bosshardt, J. Davies, R. Egli, M.-P. Ginebra, P. Habibovic, W. Hofstetter, and A. Wagoner Johnson for fruitful discussions and Mathys Ltd (Bettlach, Switzerland) for their financial support.

Appendix A. Supplementary data

Supplementary data associated with this article can be found, in the online version, at doi:10.1016/j.mattod.2017.02.002.

References

[1] E. Hernlund, et al. Arch. Osteoporosis 8 (1–2) (2013) 136.
[2] A. Wennerberg, T. Albrektsson, Clin. Oral Implants Res. 20 (Suppl. 4) (2009) 172.
[3] J.E. Davies, J. Dent. Educ. 67 (8) (2003) 932.
[4] S.F. Hulbert, et al. J. Biomed. Mater. Res. 4 (3) (1970) 433.
[5] V. Karageorgiou, D. Kaplan, Biomaterials 26 (27) (2005) 5474.
[6] O. Chan, et al. Acta Biomater. 8 (7) (2012) 2788.
[7] S.K. Lan Levengood, et al. Biomaterials 31 (13) (2010) 3552.
[8] J.E. Davies, et al. Bioceramics 4 (1991) 199.
[9] M.J. Coathup, et al. J. Biomed. Mater. Res. A 100A (6) (2012) 1550.
[10] M.F. Basle, et al. J. Mater. Sci. Mater. Med. 4 (3) (1993) 273.
[11] N. Kondo, et al. Biomaterials 27 (25) (2006) 4419.
[12] A. Bernstein, et al. Acta Biomater. 9 (7) (2013) 7490.
[13] S.J. Polak, et al. Acta Biomater. 9 (8) (2013) 7977.
[14] J. Malmstroem, et al. Clin. Impl. Dent. Relat. Res. 9 (2) (2007) 79.
[15] S.J. Polak, et al. Acta Biomater. 7 (4) (2011) 1760.
[16] H. Lapczyna, et al. Eur. Cells Mater. 28 (2014) 299.
[17] M.C. von Doernberg, et al. Biomaterials 27 (30) (2006) 5186.
[18] K.M. Nuss, et al. BMC Musculoskelet. Disord. 7 (2006) 67.
[19] T. Liu, et al. Bone 56 (1) (2013) 110.
[20] M. Bohner, et al. Biomaterials 26 (2005) 6099.
[21] L.G. Galea, et al. Biomaterials 29 (24–25) (2008) 3400.
[22] G. Martinez-Criado, et al. J. Synchrotron Radiat. 23 (2016) 344.
[23] M. Langer, et al. PLoS ONE 7 (8) (2012) e35691.
[24] B. Hesse, et al. J. Bone Miner. Res. 30 (2) (2015) 346.
[25] V. Zaichick, M. Tzaphlidou, Appl. Radiat. Isot. 58 (6) (2003) 623.
[26] P.M. Davidson, et al. Biointerphases 10 (3) (2015) 1.
[27] F.M. Klenke, et al. J. Biomed. Mater. Res. A 85 (3) (2008) 777.
[28] P. Carmeliet, R.K. Jain, Nature 407 (6801) (2000) 249.
[29] S. Mishra, M.L. Knothe Tate, Anat. Rec. A: Discov. Mol. Cell. Evol. Biol. 273 (2) (2003) 752.
[30] E. Mittra, et al. J. Biomech. 38 (6) (2005) 1229.
[31] D.D. Bosshardt, R.K. Schenk, in: D. Buser (Ed.), 20 Years of Guided Bone Regeneration, Quintessence, 2009, p. 15.
[32] D.J. Kubek, et al. Microsc. Res. Tech. 73 (3) (2010) 182.
[33] P. Varga, et al. Biomech. Model. Mechanobiol. 14 (2) (2015) 267.
[34] H. Winet, et al. J. Bone Miner. Res. 5 (1) (1990) 19.
[35] M. Bashoor-Zadeh, et al. Acta Biomater. 6 (3) (2010) 864.
[36] H. Yuan, et al. Proc. Natl. Acad. Sci. U. S. A. 107 (31) (2010) 13614.
[37] D. Apelt, et al. Biomaterials 25 (7–8) (2004) 1439.
[38] M. Bohner, J. Lemaitre, Biomaterials 30 (12) (2009) 2175.
[39] G. Vereecke, J. Lemaitre, J. Cryst. Growth 104 (1990) 820.
[40] S.L. Teitelbaum, Science 289 (5484) (2000) 1504.
[41] S. Kotani, et al. J. Biomed. Mater. Res. 25 (10) (1991) 1303.
[42] R. Xin, et al. Biomaterials 26 (33) (2005) 6477.
[43] H.O. Mayr, et al. Acta Biomater. 9 (1) (2013) 4845.